



Ab initio calculations of the $2p_{3/2}$ - $2p_{1/2}$ fine-structure splitting in boronlike ions

A. N. Artemyev,^{1,2} V. M. Shabaev,³ I. I. Tupitsyn,³ G. Plunien,⁴ A. Surzhykov,¹ and S. Fritzsche^{1,5}

¹Helmholtz-Institut Jena, Fröbelstieg 3, D-07743 Jena, Germany

²Physikalisches Institut, Universität Heidelberg, Im Neuenheimerfeld 226, D-69120 Heidelberg, Germany

³Department of Physics, St. Petersburg State University, Oulianovskaya 1, Petrodvorets, St. Petersburg 198504, Russia

⁴Institut für Theoretische Physik, TU Dresden, Mommsenstraße 13, D-01062 Dresden, Germany

⁵Theoretisch-Physikalisches Institut, Friedrich-Schiller-Universität Jena, Max-Wien-Platz 1, D-07743 Jena, Germany

(Received 24 August 2013; published 30 September 2013)

We have performed *ab initio* QED calculations of the $(1s)^2(2s)^22p_{3/2}$ - $(1s)^2(2s)^22p_{1/2}$ fine-structure splitting along the boron isoelectronic sequence for all ions with $17 \leq Z \leq 100$. This level splitting was evaluated within the extended Furry picture and by making use of four different screening potentials in order to estimate the effects of interelectronic correlations. The accuracy of the predicted transition energies has been improved significantly when compared with previous computations.

DOI: [10.1103/PhysRevA.88.032518](https://doi.org/10.1103/PhysRevA.88.032518)

PACS number(s): 31.30.jf, 31.10.+z

I. INTRODUCTION

Today, quantum electrodynamics (QED) is known as the most accurate theory for calculating the level structure and properties of atomic few-electron systems. This theory enables one to derive rigorous formulas and to compute various properties of atoms and ions, such as level energies, transition probabilities, hyperfine parameters, or the g factor of bound-state electrons in highly charged ions, just to name a few. In practice, however, various difficulties arise and often hamper the computations within the rigorous QED formalism. For the middle- and high- Z systems, for example, the calculations should be performed for all orders in αZ (with $\alpha \approx 1/137$ being the fine-structure constant), but today, yet only the two lowest orders in α are accessible for numerical computations.

The largest difficulty in calculating many-electron systems arises from the interelectronic interaction, and this problem rapidly enhances as more electrons get involved in the computations. For ions with three or more electrons, therefore, computational techniques are usually required that help merge the advantages of the *ab initio* QED theory with techniques from relativistic atomic structure theory, such as the relativistic configuration interaction (CI) or the multiconfigurational Dirac-Fock (DF) methods. Although these “atomic-structure” techniques are typically restricted to the *no-virtual-pair* approximation, they allow incorporating the interelectronic interaction within the Breit approximation to a high order or even to all orders.

In order to explore the power and feasibility of such merged techniques, the electric dipole forbidden $2p_{3/2}$ - $2p_{1/2}$ transition in boronlike ions may serve as a very good test bed. Namely, whereas, the fine-structure splitting between these (two) levels is a pure relativistic effect and with *no* nonrelativistic counterpart, the boronlike ions are still relatively simple and, hence, enable one to incorporate the interelectronic interaction with third and higher orders. Therefore, the relativistic and QED corrections are not masked in this case by the often dominating nonrelativistic contributions. In addition, highly accurate measurements of the $2p_{3/2}$ - $2p_{1/2}$ fine-structure splitting have become available during recent years. For boronlike argon, for example, this level splitting has been measured with an unprecedented relative accuracy of 10^{-7} [1–3], and

the further development of a trapping technique for highly charged ions will also likely allow extending such precision experiments towards heavy ions [4].

In Ref. [5], we have elaborated the method for many-electron calculations that combines the relativistic CI and *ab initio* QED techniques. This approach was applied successfully in this reference in order to compute the energy of the $2p_{3/2}$ - $2p_{1/2}$ forbidden transition in boronlike argon with a four times higher accuracy than in previous computations. In the present paper, we extend these calculations to all ions along the boron isoelectronic sequence with nuclear charge $17 \leq Z \leq 100$.

The paper is organized as follows. In the next section, we describe the basic formalism and present the general formulas for the calculations of level energies. In Sec. III, we then give further details of our numerical procedure as applied in the evaluations of the various QED and many-body contributions. This especially includes a brief description of an approach for calculating the one-electron self-energy (SE) diagram, whereas, all other details about the evaluation of the first- and second-order corrections to the free-electron Green’s function are deferred to the Appendix below. The numerical results of our calculations are then presented in Sec. IV, and a brief summary is given in Sec. V. Relativistic units ($\hbar = c = m = 1$) are used throughout this paper if not stated otherwise.

II. BASIC FORMULAS

The Furry picture is traditionally used in QED calculations to describe the properties of heavy highly charged ions. For zeroth order, this picture treats the electrons as moving in the Coulomb field of the nucleus only and not interacting with each other. The wave function of each individual electron, therefore, is the solution of the Dirac equation with the potential of the extended nucleus V_{nuc} ,

$$[-i\boldsymbol{\alpha} \cdot \boldsymbol{\nabla} + \beta m + V_{\text{nuc}}(\mathbf{r})]\psi_n(\mathbf{r}) = \varepsilon_n \psi_n(\mathbf{r}). \quad (1)$$

The interelectronic interaction and the coupling to the quantized electromagnetic field is then accounted for by the perturbation theory. Of course, such an approach works well if the interelectronic interaction is small when compared to

the binding energies of all electrons involved, whereas, its convergence is often slow for the case of strong interelectronic interactions.

The convergence of the perturbation series can be accelerated by replacing the nuclear potential in the Dirac equation with an effective potential that partially accounts for the screening of the nuclear potential by the other electrons,

$$V_{\text{nuc}}(r) \rightarrow V_{\text{eff}}(r) = V_{\text{nuc}}(r) + V_{\text{scr}}(r). \quad (2)$$

Then, to avoid the double counting of the screening contributions, the interaction with $-V_{\text{scr}}(r)$ must be added perturbatively.

In this paper, we have used four different screening potentials whose choice will be discussed below. For the moment, let us just mention here that the calculation of the $(1s)^2(2s)^22p$ level energies is difficult in a *pure* Coulomb field (or even by including a finite size of the nucleus) because of the (quasi)degeneracy of the $(1s)^2(2s)^22p_{3/2}$ and $(1s)^2(2p_{1/2})^22p_{3/2}$ levels. The use of some screening potential removes this degeneracy and significantly simplifies the derivation of the basic formulas, making both $(1s)^2(2s)^22p$ levels isolated with regard to other levels of the same symmetry.

A. Interelectronic interaction within the QED approach

The calculations of the $2p_{3/2}-2p_{1/2}$ transition energy can conveniently be performed in a few separate steps. First, we will calculate those parts that correspond to the Feynman diagrams *without* any photon or electron loops, and as they naturally arise in both, the standard QED and non-QED approaches. These diagrams are shown in Fig. 1. The dashed lines with triangles at the ends refer to the local potential V_{scr} , that was added to the Dirac Hamiltonian, but is taken here with the opposite sign in order to subtract it from the (total) interaction Hamiltonian as mentioned after Eq. (2). Since we are just interested in the $2p_{3/2}-2p_{1/2}$ transition energy, *no* diagrams occur with only core electrons as incoming (outgoing) electron lines as they will cancel each other. For this reason, here and throughout the paper, we will discuss only those diagrams where one of the incoming (outgoing) electron lines corresponds to one of the (valence) $2p$ electrons.

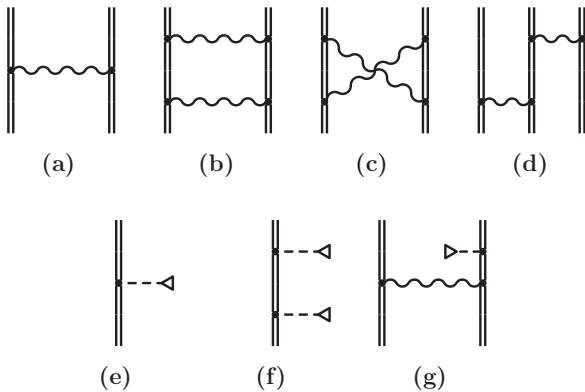


FIG. 1. The interelectronic interaction diagrams. The double lines denote the bound electrons moving in the effective potential (2), whereas, the dashed lines with triangles denote the total screening potential but taken with the opposite sign.

The formulas for calculating diagrams (a)–(d) in Fig. 1 can be found in our previous papers on the two-photon exchange corrections to the energy levels of lithiumlike ions; see, e.g., Ref. [6] for further details. Since boronlike ions have a $(1s)^2(2s)^2$ core, analog expressions as for the $1s$ core orbitals for lithiumlike ions must also be included for the $2s$ orbitals here. For the contribution of diagrams (e)–(g) in Fig. 1, one can easily obtain the following formulas:

$$\Delta E_{(e)} = V_{vv}, \quad (3)$$

$$\Delta E_{(f)} = \sum_{n \neq v} \frac{|V_{vn}|^2}{\varepsilon_v - \varepsilon_n}, \quad (4)$$

$$\begin{aligned} \Delta E_{(g)} = 2 \sum_{c=1s,2s;\mu_c} \left[\sum_{n \neq v} \sum_P (-1)^P \frac{I_{PcPvcn}(\varepsilon_{Pc} - \varepsilon_c) V_{nv}}{\varepsilon_v - \varepsilon_n} \right. \\ \left. + \sum_{n \neq c} \sum_P (-1)^P \frac{I_{PcPvuv}(\varepsilon_{Pv} - \varepsilon_v) V_{nc}}{\varepsilon_c - \varepsilon_n} \right] \\ - \sum_{n=c} (V_{vv} - V_{nn}) I'_{vnnv}(\varepsilon_v - \varepsilon_n). \end{aligned} \quad (5)$$

For the sake of brevity, here we introduced the following notations: $V_{ab} = \langle a | -V_{\text{scr}} | b \rangle$, $I_{abcd}(\omega) = \langle ab | I(\omega) | cd \rangle$, $I(\omega) = e^2 \alpha^\mu \alpha^\nu D_{\mu\nu}(\omega)$, and $I'_{abcd}(\omega) = \langle ab | \frac{\partial}{\partial \omega} I(\omega) | cd \rangle$, where D denotes the photon propagator, P denotes the permutation operator, and $(-1)^P$ denotes the sign of the permutation. In all these expressions, c refers to the wave functions of the (one-electron) core states ($1s$ or $2s$), whereas, v denotes the valence ($2p$) states, and n runs over all possible solutions of the one-electron Dirac equation with the given effective potential Eq. (2).

B. QED corrections

Apart from the diagrams in Fig. 1 for the interelectronic interaction, one has to evaluate the diagrams that arise only within a rigorous QED approach. Figure 2 displays all QED diagrams that are presently available for numerical computations. Note that the set of second-order diagrams is not yet complete since it omits the one-electron two-loop diagrams; the contribution of these diagrams will be discussed below in Sec. II D.

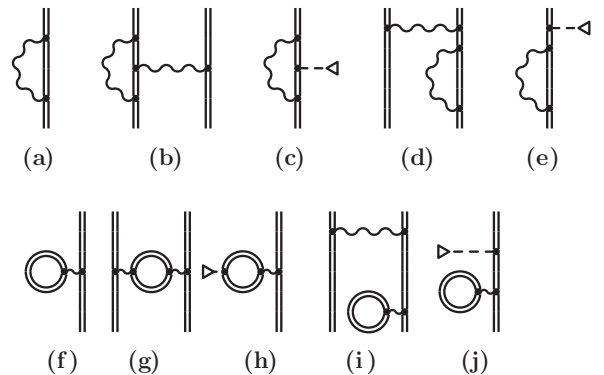


FIG. 2. First- and second-order QED diagrams (without the one-electron two-loop diagrams) for systems with a single valence electron. The notation is the same as in Fig. 1.

The first-order diagrams are shown in Figs. 2(a) and 2(f). These diagrams are known as one-loop self-energy (SE) and vacuum-polarization (VP) diagrams. For H-like ions, the SE diagram was calculated first by Mohr [7,8], whereas, the VP diagram was calculated by Soff and Mohr [9] and by Manakov *et al.* [10]. Formally, the expressions for these two diagrams look rather simple if we introduce the SE operator $\Sigma(\epsilon)$ and the VP potential U_{VP} as follows:

$$\langle a|\Sigma(\epsilon)|b\rangle = \frac{i}{2\pi} \int_{-\infty}^{\infty} d\omega \sum_n \frac{\langle a|e^2\alpha^\mu\alpha^\nu D_{\mu\nu}(\omega)|nb\rangle}{\epsilon - \omega - \epsilon_n(1-i)}, \quad (6)$$

$$U_{VP}(\mathbf{x}) = \frac{\alpha}{2\pi i} \int d\mathbf{r}' \frac{1}{|\mathbf{r}' - \mathbf{r}|} \int_{-\infty}^{\infty} d\omega \text{Tr}[G(\omega; \mathbf{r}, \mathbf{r}')], \quad (7)$$

where $G(\omega; \mathbf{r}, \mathbf{r}')$ is the bound-electron Green's function and $D_{\mu\nu}$ is the photon propagator.

With these operators at hand, the formulas for the energy contributions of the electron's self-energy and vacuum

polarization can simply be written in the form

$$\Delta E_{SE} = \langle v|\Sigma(\epsilon_v)|v\rangle, \quad (8)$$

$$\Delta E_{VP} = \langle v|U_{VP}|v\rangle. \quad (9)$$

However, both the SE and the VP contributions are divergent; they become finite only after renormalization. The procedure of the renormalization is well known and has been described elsewhere; see Refs. [7,9,11–13] for details.

All the other diagrams in Fig. 2 represent the so-called *screened* QED corrections. These diagrams can conveniently be split into some irreducible part in which the energy of the intermediate state differs from the energy of the initial (final) state and some reducible part to cover the remaining contributions. This decomposition and the formulas for diagrams (b), (d), (g), and (i) in Fig. 2 can be found, for example, in our previous paper [14]. The derivation of the formulas for the diagrams (c), (e), (h), and (j) yields (see, e.g., Ref. [15]),

$$\Delta E_{(c)} = \frac{i}{2\pi} \int_{-\infty}^{-\infty} d\omega \sum_{n_1, n_2} \frac{V_{n_1 n_2} I_{v n_2 n_1 v}(\omega)}{[\epsilon_v - \omega - \epsilon_{n_1}(1-i0)][\epsilon_v - \omega - \epsilon_{n_2}(1-i0)]}, \quad (10)$$

$$\Delta E_{(e)} = 2\langle v|\Sigma(\epsilon_v)|\xi_v\rangle + V_{vv}\langle v|\Sigma'(\epsilon_v)|v\rangle, \quad (11)$$

$$\Delta E_{(h)} = \frac{1}{2\pi i} \int_{-\infty}^{-\infty} d\omega \sum_{n_1, n_2} \frac{V_{n_1 n_2} I_{v n_2 v n_1}(0)}{[\epsilon_v - \omega - \epsilon_{n_1}(1-i0)](\epsilon_v - \omega - \epsilon_{n_2}(1-i0))}, \quad (12)$$

$$\Delta E_{(j)} = 2\langle v|U_{VP}|\xi_v\rangle. \quad (13)$$

Here, we have introduced the correction to the wave function of the valence electron,

$$|\xi_v\rangle = \sum_{n \neq v} \frac{V_{vn}|n\rangle}{\epsilon_v - \epsilon_n}, \quad (14)$$

owing to the screening potential. Further details of the numerical evaluation of these diagrams will be discussed in the next section.

C. Third and higher orders of the interelectronic interaction

In the previous subsections, we explained how the expressions of the first- and second-order QED diagrams can be found for systems with a single valence electron. As pointed out before, however, third- and higher-order contributions from the electron-electron interaction also are important and need to be evaluated at least within the Breit approximation. In the third step of the present computations, we have evaluated these contributions by means of the relativistic configuration-interaction Dirac-Fock-Sturm (CI-DFS) method [16]. The following procedure has been employed in order to extract the desired contributions from the CI-DFS data. We represent the Hamiltonian of the CI-DFS calculations in the form

$$H = H_0 + \lambda H_{\text{int}}, \quad (15)$$

where H_0 is the sum of the one-electron Dirac Hamiltonians with the effective potential (2) and H_{int} accounts for the

interaction of the electrons with each other and with $-V_{\text{scr}}$. Moreover, here, λ is an arbitrary parameter so that H coincides with the exact Hamiltonian for $\lambda = 1$. In this representation, the energy E becomes a function of the parameter λ , and one can use the expansion of E in powers of λ ,

$$E = E^{(0)} + \lambda E^{(1)} + \lambda^2 E^{(2)} + E^{(\geq 3)}(\lambda). \quad (16)$$

In this expression, $E^{(\geq 3)}(\lambda) = O(\lambda^3)$ denotes all terms of the third and higher orders in λ . It can be seen that the coefficient $E^{(1)}$ corresponds to the contribution of diagrams (a) and (e) in Fig. 1 and the coefficient $E^{(2)}$ corresponds to diagrams (b), (d), (f), and (g). In the Coulomb gauge, which is generally used to derive the Dirac-Coulomb-Breit Hamiltonian, diagram (c) contributes only beyond the Breit approximation.

In some more detail, the coefficients $E^{(0)}$, $E^{(1)}$, and $E^{(2)}$ can be extracted numerically from the CI-DFS calculations as follows:

$$E^{(0)} = \lim_{\lambda \rightarrow 0} E, \quad (17)$$

$$E^{(1)} = \lim_{\lambda \rightarrow 0} \frac{E - E^{(0)}}{\lambda}, \quad (18)$$

$$E^{(2)} = \lim_{\lambda \rightarrow 0} \frac{E - E^{(0)} - \lambda E^{(1)}}{\lambda^2}. \quad (19)$$

Thereafter, the coefficient $E^{(\geq 3)}$ is calculated and for $\lambda = 1$ represents the contribution of the interelectronic interaction in third and higher orders within the Breit approximation. In

addition, in order to estimate the accuracy of this (numerical) procedure, we have calculated the diagrams (a), (b), and (d)–(g) by using our code for the QED calculations described in Sec. II A but within the (low-frequency) Breit approximation only, i.e., by neglecting the frequency-dependent part of the photon propagator in the Coulomb gauge as well as all contributions from the negative energy continuum. The obtained results have been compared with the coefficients $E^{(1)}$ and $E^{(2)}$ as extracted from the CI-DFS calculations, and very good agreement was found between these numbers from two different codes and for all four screening potentials.

D. Two-loop one-electron diagrams and recoil contributions

To complete the rigorous QED treatment of the $2p_{3/2}$ – $2p_{1/2}$ transition energy in *second* order in α , one has to also evaluate the two-loop one-electron diagrams. The full treatment of these diagrams is a very demanding task, which has not been solved yet in all orders in αZ , even for the simplest case of H-like ions in their ground states. Recent progress in this treatment has been achieved by Yerokhin and co-workers who evaluated the complete set of two-loop self-energy diagrams for $2p$ states of hydrogenlike ions [17] and performed the evaluation of the rest of the two-loop diagrams [18] using the so-called *free-loop approximation* if the complete calculations were impossible. To incorporate the contribution of one-electron two-loop diagrams into our calculations for nuclear charges $Z \geq 60$, we interpolated the data obtained in Refs. [17,18]. For lower values of Z , the evaluation of the complete set of diagrams has not yet been performed. Therefore, we estimated this contribution by using the analytical αZ expansion as reported in Ref. [19].

The calculation of the nuclear recoil corrections has been performed for all orders in αZ using the same approach as in our recent paper [2] in which the isotope shift of the forbidden transition energies of boron- and berylliumlike argon has been investigated.

III. NUMERICAL EVALUATION

Having derived the basic formulas, we are now prepared to describe the details of the numerical computation of the $2p_{3/2}$ – $2p_{1/2}$ transition energy.

A. Choice of the screening potential

As mentioned above, the evaluation of the $2p_{3/2}$ – $2p_{1/2}$ transition energy becomes quite complicated if one starts from the Hamiltonian of the noninteracting electrons. There are two reasons for this difficulty. On one hand, the $2s$ and $2p_{1/2}$ one-electron states are degenerate in a pure Coulomb field of the nucleus and, thus, the levels of the five-electron configurations $(1s)^2(2s)^22p_{3/2}$ and $(1s)^2(2p_{1/2})^22p_{3/2}$ are degenerate in the lowest order. This requires formulating the perturbation theory for some degenerate level space and significantly complicates the derivation of the formulas. On the other hand, the interelectronic interaction in boronlike ions is generally not small for low- and middle- Z ions when compared to the electron-nucleus one. This fact slows down the convergence of the perturbation expansion with initially noninteracting electrons. In order to accelerate this convergence, one may start

from some effective potential that partially incorporates the screening effects into the unperturbed Hamiltonian. The better this potential approximates the interelectronic interaction in the bound-state density, the faster the perturbation series is expected to converge.

There are different ways to choose the effective potential for the ground state of an atom or ion. In the present paper, we have employed four different screening potentials.

Our first choice of the potential is sometimes called the core-Hartree potential V_{CH} , which is obtained as a self-consistent solution of the Dirac equation with the potential,

$$V(\mathbf{r}) = V_{\text{nuc}}(\mathbf{r}) + \alpha \sum_{n=1s,2s} \int d\mathbf{r}' \frac{|\psi_n(\mathbf{r}')|^2}{|\mathbf{r} - \mathbf{r}'|}. \quad (20)$$

This potential includes the interaction of the electrons with the nucleus as well as the averaged Coulomb interaction of an electron with the core electrons.

Another potential is generated directly from the wave functions of the $(1s)^2(2s)^22p$ states obtained within the Dirac-Fock approximation. We will call this potential the local Dirac-Fock potential V_{LDF} ; it reproduces the energies and wave functions of the $2p$ states at the DF level or better. The potential V_{LDF} is then constructed by inversion of the radial Dirac equation with the radial wave functions obtained in the DF computations [20].

Two other potentials were obtained by using density-functional-theory techniques. The Perdew-Zunger potential V_{PZ} has been widely used in molecular and cluster computations and has been described in Ref. [21]. In the well-known Slater potential V_{Sl} , finally, the exchange interaction of the electrons is expressed in terms of the one-electron (radial) density [22],

$$\rho_t(r) = 4\pi r^2 \rho(r), \quad (21)$$

$$\int \rho(r) d^3r = \int_0^\infty \rho_t(r) dr = N, \quad (22)$$

where N is the total number of the electrons. With these definitions, one can represent the Slater potential in the simple form

$$V_{\text{Sl}}(r) = V_{\text{nuc}}(r) + \alpha \int_0^\infty \frac{\rho_t(r')}{\max(r, r')} dr' - x_\alpha \frac{\alpha}{r} \left(\frac{81}{32\pi^2} r \rho_t(r) \right)^{1/3}. \quad (23)$$

In fact, this equation gives rise to a whole set of potentials which just differ in the value of the constant x_α . Following Slater's original paper [22], we chose $x_\alpha = 1$. Note that ρ_t in Eq. (21) denotes the total one-electron density including the charge densities of the core and valence electrons. This is in contrast to the core-Hartree potential that only includes the density of the core electrons. Because of this difference, the Slater potential decreases for large radii $r \rightarrow \infty$ as $-\alpha \frac{Z-N}{r}$ and with $N = 5$ for the boronlike ions. Since we are interested in the behavior of the valence $2p$ electron in the screened field of the nucleus, we added the self-interaction or (so-called) Latter correction to this potential [23] in order to obtain the correct asymptotic form $-\alpha \frac{Z-N+1}{r}$.

B. Self-energy computations

Once the screening potentials are selected and the associated one-electron spectra are evaluated, we can carry out all further computations within the extended Furry picture following analog lines as in our previous calculations of helium- and lithiumlike ions. The analytical expressions for these computations are derived in Sec. II, and the numerical treatment of most contributions is very similar to those in our previous papers; cf. Refs. [6,14] and references therein.

One of the building blocks for any successful QED calculation within the extended Furry picture is the Green's function of an electron moving in the field of the *screened* nuclear potential. As pointed out above, this screened potential removes the degeneracy between the $2s$ and the $2p$ (one-electron) states and improves the convergence of the perturbation series. However, whereas, this Green's function is well known analytically for a pure Coulomb field (of a pointlike nucleus) and for a homogeneously charged spherical shell field, such analytical solutions are not available for an arbitrary external (screening) potential. Therefore, in order to evaluate the Green's function for such a potential, one has either to find them numerically, solving a corresponding system of differential equations, or to apply a spectral decomposition,

$$G(\omega) = \sum_n \frac{|n\rangle\langle n|}{\omega - \varepsilon_n(1 - i0)}, \quad (24)$$

where the summation runs over the complete Dirac spectrum. We have applied both approaches in this paper. For the VP diagram in Fig. 2(f), for example, the Green's function $G(\omega)$ has been calculated numerically, whereas, a spectral decomposition within a B -spline basis set [24,25] was used to evaluate the SE diagram in Fig. 2(a). The main reason for this (slightly) different numerical treatment of the VP and SE contributions was the availability of the codes already tested in similar calculations but without using some screening potentials.

For a wide range of nuclear charges $17 \leq Z \lesssim 90$, the one-electron self-energy diagram in Fig. 2(a) is the leading QED contribution to the $2p_{3/2}$ - $2p_{1/2}$ transition energy. For boronlike ions, however, we could not follow the *standard* numerical procedure as applied in Ref. [25] and shown in the upper line of Fig. 3. In this figure, the lines with the crosses at the ends denote the interaction with the effective potential V_{eff} (2), i.e., the sum of the nuclear and screening potentials. The standard (upper) expansion in Fig. 3 gives rise to zero- and first-order terms $\Delta E_0^{\text{SE}} + \Delta E_1^{\text{SE}}$, that are both divergent. These two terms should be renormalized together with the mass-counter term and should be calculated within the momentum representation (see Ref. [26] for details). The remaining higher-order term $\Delta E_{\geq 2}^{\text{SE}}$ is convergent and usually is calculated in the coordinate space by using a partial-wave decomposition for the electron propagators.

Making use of this decomposition (in the upper line of Fig. 3) for the SE evaluation for the $2p$ electron, we found that the partial-wave expansion of the higher-order term $\Delta E_{\geq 2}^{\text{SE}}$ converges very slowly for all middle- Z elements. This made it impossible to apply the B -spline method for generating a spectral representation of the Green's function because of the very rapid increase in the number of B splines for high angular quantum numbers κ . For such high values of κ , one

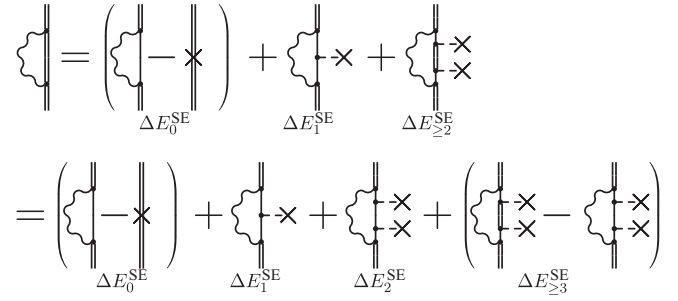


FIG. 3. Decomposition of the one-electron self-energy diagram into various contributions. Whereas, the upper line represents the traditional decomposition by means of a zero-, first-, and higher-order term $\Delta E_0^{\text{SE}} + \Delta E_1^{\text{SE}} + \Delta E_{\geq 2}^{\text{SE}}$, the lower line is used in the present paper. It gives rise to a second-order term ΔE_2^{SE} , which is calculated by using the analytical representation of the free-electron Green's function and a higher-order term $\Delta E_{\geq 3}^{\text{SE}}$. This decomposition ensures an improved convergence and, thus, makes the second-order SE computation feasible for many-electron ions; see Sec. III B for further details. The dashed lines with crosses at the ends denote the sum of the nuclear and screening potentials.

needs to use an enormously large number of B splines in order to obtain an adequate representation of the Green's function. Moreover, the numerical evaluation of the radial components of the Green's function also becomes very ineffective for large angular momentum quantum numbers.

For these reasons, we had to modify the traditional decomposition of the SE diagram in Fig. 3. An alternative scheme is shown in the lower line of this figure in which the slowly convergent part of $\Delta E_{\geq 2}^{\text{SE}}$, that involves two external potentials, is separated and is calculated in coordinate space by using the analytical representation for the *free-electron* propagator. The details of this decomposition are presented in the Appendix. For the modified higher-order term $\Delta E_{\geq 3}^{\text{SE}}$, a fast convergence with the number of partial waves was found, and this (remaining) term was calculated by means of the B -spline method.

To demonstrate the capability of this *revised* decomposition, the SE diagram has been calculated for the $2p_{1/2}$ and $2p_{3/2}$ states of hydrogenlike argon with a pointlike nucleus. In Tables I and II, we display the partial-wave contributions to the one-electron self-energy of hydrogenlike argon. In particular, we show how the second-order term ΔE_2^{SE} in Fig. 3 (Table I) and the higher-order term $\Delta E_{\geq 3}^{\text{SE}}$ (Table II) converge as functions of κ , the angular momentum quantum number of the partial waves. As seen from these tables, ΔE_2^{SE} converges much slower than the modified higher-order term $\Delta E_{\geq 3}^{\text{SE}}$. Apparently, even 100 partial waves ($-50 \leq \kappa \leq 50$) are not yet sufficient to achieve good accuracy for the second-order term ΔE_2^{SE} alone, whereas, just about 10 partial waves are enough if the cancellation of the second- and higher-order contributions is taken into account as this is performed by the modified term $\Delta E_{\geq 3}^{\text{SE}}$. In Table III, we also present the zero- and first-order terms $\Delta E_0^{\text{SE}} + \Delta E_1^{\text{SE}}$, calculated in the momentum representation. The sum of these four terms gives rise to the total self-energy ΔE^{SE} , which can be compared to the values by Mohr [27], and nicely demonstrates the accuracy of the present approach.

TABLE I. Partial-wave contributions to the second-order term ΔE_2^{SE} as displayed in the lower line of Fig. 3 for hydrogenlike argon. Values are given in units of $\frac{\alpha}{\pi} \frac{(\alpha Z)^4}{8} mc^2$.

$ \kappa $	$2p_{1/2}$	$2p_{3/2}$	$2p_{1/2}-2p_{3/2}$
1	48.6150	2.2870	46.32799
2	3.7808	47.1729	-43.39209
3	1.2057	3.1191	-1.91341
4	0.5769	0.9464	-0.36951
5	0.3304	0.4493	-0.11888
6	0.2095	0.2588	-0.04935
7	0.1419	0.1658	-0.02389
8	0.1008	0.1137	-0.01283
9	0.0742	0.0816	-0.00743
10	0.0562	0.0607	-0.00457
11...20	0.2021	0.2117	-0.00954
21...30	0.0409	0.0416	-0.00071
31...40	0.0138	0.0140	-0.00015
41...50	0.0061	0.0061	-0.00005
> 50	0.0075(20)	0.0075(20)	-0.00001
Total	55.3617(20)	54.9361(20)	0.42558

C. Vacuum-polarization computations

Figure 2(f) shows the one-electron vacuum-polarization diagram as it appears in the lowest order in α . For electrons in an effective potential, it is convenient to consider this diagram together with diagram (h) from the same figure. Both diagrams can be computed in the traditional approach [9] by a decomposition of the vacuum loop electron propagator in powers of the external potential. In this expansion, the first nonvanishing (also called the Uehling) term contains either *one* interaction with the full effective potential [diagram (f)] or with its screening part only but then with the opposite sign [diagram (h)]. Since the sum of these two potentials is just equal to the electron-nucleus interaction, the two diagrams (f) and (h) in Fig. 2 give rise within the Uehling approximation to the total contribution,

$$\Delta E_{(f)+(h)}^{\text{Ue}} = \langle v | U_{\text{Ue}} | v \rangle. \quad (25)$$

TABLE II. The same as in Table I but for the higher-order term $\Delta E_{\geq 3}^{\text{SE}}$ in Fig. 3.

$ \kappa $	$2p_{1/2}$	$2p_{3/2}$	$2p_{1/2}-2p_{3/2}$
1	59.2891	0.5039	58.78517
2	0.3770	58.3431	-57.96609
3	0.0552	0.3133	-0.25805
4	0.0172	0.0420	-0.02482
5	0.0073	0.0127	-0.00535
6	0.0037	0.0054	-0.00169
7	0.0021	0.0027	-0.00066
8	0.0013	0.0016	-0.00030
9	0.0008	0.0009	-0.00015
10	0.0005	0.0006	-0.00008
> 10	0.0015(3)	0.0017(3)	-0.00015(3)
Total	59.7557(3)	59.2279(3)	0.52782(3)

TABLE III. Individual contributions to the one-electron self-energy in hydrogenlike argon. All values are shown in units of $\frac{\alpha}{\pi} \frac{(\alpha Z)^4}{8} mc^2$.

	$2p_{1/2}$	$2p_{3/2}$	$2p_{1/2}-2p_{3/2}$
ΔE_0^{SE}	-547.0716	-543.5282	-3.54333
ΔE_1^{SE}	431.8547	429.5031	2.35160
ΔE_2^{SE}	55.3617(20)	54.9361(20)	0.42558
$\Delta E_{\geq 3}^{\text{SE}}$	59.7557(3)	59.2279(3)	0.52782(3)
ΔE^{SE}	-0.0995(20)	0.1389(20)	-0.23831(3)
Ref. [27]	-0.09751	0.14082	-0.23833

In this expression, the Uehling potential needs to be calculated just for the nuclear charge density $\rho_n(r)$,

$$U_{\text{Ue}}(r) = -\frac{8}{3} \alpha^2 Z \int_0^\infty dr' r' \rho_n(r') \times \int_1^\infty dt \left(1 + \frac{1}{2t^2}\right) \frac{\sqrt{t^2 - 1}}{t^2} \times \frac{\exp(-2|r - r'|t) - \exp[-2(r + r')t]}{4rt}. \quad (26)$$

The calculation of the remaining part of the VP diagrams (f) and (h) in Fig. 2, also known as the Wichmann-Kroll contribution, has been performed following our previous paper [28]. This is achieved by the partial-wave decomposition of the electron propagator and the subsequent evaluation of the difference between the diagram as a whole and the first nonvanishing (Uehling) term in coordinate space. These computations require the evaluation of the bound-electron Green's function, which was performed by using the numerical solution of the corresponding differential equations.

D. Screened QED diagrams

The screened QED contributions to the transition energy are defined by the diagrams displayed in Fig. 2 [diagrams (b)–(e) for the screened self-energy and diagrams (g), (i), and (j) for the screened vacuum polarization]. Let us recall here that diagram (h) has already been considered together with diagram (f) in Sec. III C. The evaluation of the screened vacuum-polarization diagrams (i) and (j) is relatively simple owing to the fact that these diagrams contain the local vacuum-polarization potential. Once this potential has been generated, the evaluation of these two diagrams can be performed in the same way as diagrams (f) and (g) in Fig. 1, replacing the screening potential hereby with the vacuum-polarization potential. Moreover, the calculation of diagram (g) in Fig. 2 can be performed in the same way as the one-photon exchange diagram (a) in Fig. 1 by replacing the photon propagator $I(\omega)$ with the modified photon propagator (within the Uehling approximation),

$$I_{\text{VP}}^{(g)}(\omega; \mathbf{r}, \mathbf{r}') = \alpha \frac{\alpha_{1\mu} \alpha_2^\mu}{|\mathbf{r} - \mathbf{r}'|} \frac{2\alpha}{3\pi} \int_1^\infty dt \left(1 + \frac{1}{2t^2}\right) \frac{\sqrt{t^2 - 1}}{t^2} \times \exp(-\sqrt{4t^2 - \omega^2} |\mathbf{r} - \mathbf{r}'|). \quad (27)$$

Here, the Uehling approximation is just enough to compute diagram (g) since the remaining Wichmann-Kroll contribution

is known to be negligible (on the order of 10^{-3} eV for lithium-like uranium), cf. our previous paper [29].

The computation of the *screened* SE diagrams in Fig. 2 can be conveniently split into the calculations of the vertex and wave-function correction terms. The irreducible part of diagrams (d) and (e), for which the energy of the intermediate

state is not equal to the energy of the initial (final) state, can easily be expressed in terms of a wave-function correction to diagram (a) and can be calculated with formulas found in Ref. [30].

For the vertex diagrams (b) and (c) in Fig. 2, the following formulas were derived by Yerokhin and co-workers [30]:

$$\begin{aligned} \Delta E_{\text{ver}} = & \sum_{c=1s,2s} \sum_{\mu\nu} \sum_P (-1)^P \sum_{n_1 n_2} \frac{i}{2\pi} \int_{-\infty}^{\infty} d\omega \left[\frac{I_{n_1 P v n_2 v}(\varepsilon_v - \varepsilon_P v) I_{P c n_2 n_1 c}(\omega)}{[\varepsilon_{Pc} - \omega - \varepsilon_{n_1}(1-i0)][\varepsilon_c - \omega - \varepsilon_{n_2}(1-i0)]} \right. \\ & \left. + \frac{I_{n_1 P c c n_2}(\varepsilon_{Pc} - \varepsilon_c) I_{P v n_2 n_1 v}(\omega)}{[\varepsilon_{Pv} - \omega - \varepsilon_{n_1}(1-i0)][\varepsilon_v - \omega - \varepsilon_{n_2}(1-i0)]} \right] + \sum_{n_1 n_2} \frac{i}{2\pi} \frac{V_{n_1 n_2} I_{v n_2 n_1 v}(\omega)}{[\varepsilon_{Pv} - \omega - \varepsilon_{n_1}(1-i0)][\varepsilon_v - \omega - \varepsilon_{n_2}(1-i0)]}, \quad (28) \end{aligned}$$

where P is the permutation operator and $(-1)^P$ is the sign associated with this permutation.

Formula (28) is just a formal expression. It contains both ultraviolet and infrared divergences. The traditional way to calculate such vertex diagrams is to isolate the ultraviolet-divergent part of the free-electron propagator and to calculate it in momentum representation once the renormalization has been performed. The remaining part of the diagrams can then be calculated by summing the partial-wave differences between the total expression and the related expression with the bound-electron propagators replaced by the free-electron ones. In this summation, only a few infrared-divergent terms with poles of second order at $\omega = 0$ appear, and these terms should be calculated together with the infrared-divergent terms of diagrams (d) and (e) in Fig. 2. Since these divergences cancel each other, the sum of the remaining terms converges and describes the physical part of the corresponding self-energy diagrams; see Ref. [30] for further details.

To accelerate the computations, i.e., the convergence of the sum over the partial waves, the following procedure has been applied. Since Eq. (28) contains a double summation over n_1 and n_2 , the CPU time can be reduced considerably if we can rewrite it in a form where the two summations are carried out independent of each other. For example, let us consider the direct part of the first term in Eq. (28). To remove the double summation over n_1 and n_2 , we may rewrite this term as follows:

$$\begin{aligned} \sum_{n_1 n_2} \frac{I_{n_1 v n_2 v}(0) I_{c n_2 n_1 c}(\omega)}{[\varepsilon_c - \omega - \varepsilon_{n_1}(1-i0)][\varepsilon_c - \omega - \varepsilon_{n_2}(1-i0)]} &= \sum_{n_1=n_2} \frac{I_{n_1 v n_1 v}(0) I_{c n_1 n_1 c}(\omega)}{[\varepsilon_c - \omega - \varepsilon_{n_1}(1-i0)]^2} \\ &+ \sum_{n_1 \neq n_2} \frac{1}{\varepsilon_{n_1} - \varepsilon_{n_2}} \left[\frac{I_{n_1 v n_2 v}(0) I_{c n_2 n_1 c}(\omega)}{[\varepsilon_c - \omega - \varepsilon_{n_1}(1-i0)]} - \frac{I_{n_1 v n_2 v}(0) I_{c n_2 n_1 c}(\omega)}{[\varepsilon_c - \omega - \varepsilon_{n_2}(1-i0)]} \right], \quad (29) \end{aligned}$$

where the first term now contains only a single summation over n_1 . If, in addition, we introduce the energy-independent effective wave functions,

$$|\tilde{n}_1\rangle = \sum_{n_2 \neq n_1} \frac{1}{\varepsilon_{n_1} - \varepsilon_{n_2}} I_{n_1 v n_2 v}(0) |n_2\rangle, \quad (30)$$

$$|\tilde{n}_2\rangle = \sum_{n_1 \neq n_2} \frac{1}{\varepsilon_{n_1} - \varepsilon_{n_2}} I_{n_1 v n_2 v}(0) |n_1\rangle, \quad (31)$$

we get

$$\begin{aligned} \sum_{n_1 n_2} \frac{I_{n_1 v n_2 v}(0) I_{c n_2 n_1 c}(\omega)}{[\varepsilon_c - \omega - \varepsilon_{n_1}(1-i0)][\varepsilon_c - \omega - \varepsilon_{n_2}(1-i0)]} &= \sum_{n_1} \frac{I_{n_1 v n_1 v}(0) I_{c n_1 n_1 c}(\omega)}{[\varepsilon_c - \omega - \varepsilon_{n_1}(1-i0)]^2} + \sum_{n_1} \frac{I_{c \tilde{n}_1 n_1 c}(\omega)}{\varepsilon_c - \omega - \varepsilon_{n_1}(1-i0)} \\ &- \sum_{n_2} \frac{I_{c n_2 \tilde{n}_2 c}(\omega)}{\varepsilon_c - \omega - \varepsilon_{n_2}(1-i0)}. \quad (32) \end{aligned}$$

Apart from the clearly reduced CPU time, this algorithm enables one to calculate the integral over the energy much more accurately and with less points for the numerical integration. The latter advantage arises from the form of the integrand for small values of the differences $\varepsilon_c - \varepsilon_{n_1, n_2}$, which possesses only one pole, instead of two poles in the initial function. A very similar approach can also be utilized for all other terms in Eq. (28).

IV. RESULTS AND DISCUSSION

Table IV displays the contributions of the individual interelectronic and QED terms to the $2p_{3/2} \text{-} 2p_{1/2}$ transition energy for four selected boronlike ions. These contributions are calculated for the four different screening potentials from Sec. III A. For each ion, the first line (E_{Dirac}) displays the difference between the one-electron energies of the $2p$ electrons as obtained from the Dirac equation with the effective

TABLE IV. Individual contributions to the $2p_{3/2}-2p_{1/2}$ transition energy in boronlike ions. Results (in eV) are shown for four selected ions and four screening potentials as described in Sec. III A. See text for details.

Ion		V_{CH}	V_{DF}	V_{PZ}	V_{SI}
Cl ¹²⁺	E_{Dirac}	2.3276	2.4226	2.3805	2.5460
	E_{Breit}^1	-0.1011	-0.2099	-0.1560	-0.3531
	E_{Breit}^2	-0.1410	-0.1188	-0.1082	-0.0952
	$E_{Breit}^{\geq 3}$	0.0686	0.0603	0.0378	0.0563
	E_{QED}^1	0.0052	0.0053	0.0053	0.0057
	E_{QED}^2	0.0003	-0.0000	0.0001	-0.0004
	E_{QED}^{2l}	-0.0000	-0.0000	-0.0000	-0.0000
	E_{rec}	-0.0001	-0.0001	-0.0001	-0.0001
	E_{total}	2.1595	2.1593	2.1594	2.1592
	Xe ⁴⁹⁺	E_{Dirac}	366.7933	371.5016	369.3500
E_{Breit}^1		-5.7788	-10.7097	-8.4134	-16.6264
E_{Breit}^2		-4.8274	-4.3985	-3.8829	-3.9515
$E_{Breit}^{\geq 3}$		1.6745	1.4625	0.8049	1.3186
E_{QED}^1		0.6084	0.6149	0.6102	0.6217
E_{QED}^2		0.0276	0.0219	0.0216	0.0163
E_{QED}^{2l}		-0.0010	-0.0010	-0.0010	-0.0010
E_{rec}		-0.0036	-0.0036	-0.0037	-0.0038
E_{total}		358.4930	358.4880	358.4857	358.4825
U ⁸⁷⁺		E_{Dirac}	4139.3664	4175.4560	4162.5556
	E_{Breit}^1	-47.1482	-84.4977	-71.2385	-128.9683
	E_{Breit}^2	-10.1432	-8.7456	-7.9234	-6.7762
	$E_{Breit}^{\geq 3}$	3.4183	3.2194	2.0756	3.0783
	E_{QED}^1	1.8786	1.8614	1.7259	1.7504
	E_{QED}^2	0.3739	0.3960	0.4014	0.4536
	E_{QED}^{2l}	-0.0234	-0.0234	-0.0234	-0.0234
	E_{rec}	-0.0383	-0.0388	-0.0389	-0.0396
	E_{total}	4087.6841	4087.6273	4087.5342	4087.5104
	Fm ⁹⁵⁺	E_{Dirac}	6290.0872	6343.1819	6326.1677
E_{Breit}^1		-69.1618	-124.0741	-106.7144	-189.8123
E_{Breit}^2		-11.7332	-9.8482	-8.7854	-7.0436
$E_{Breit}^{\geq 3}$		4.2250	4.0547	2.7093	3.9716
E_{QED}^1		0.3517	0.3225	0.0946	-0.1205
E_{QED}^2		0.6906	0.7501	0.7603	0.8932
E_{QED}^{2l}		-0.0423	-0.0423	-0.0423	-0.0423
E_{rec}		-0.0651	-0.0660	-0.0662	-0.0672
E_{total}		6214.3521	6214.2787	6214.1236	6213.8883

potential (2). The next two lines then list the contributions of the first- and second-order interelectronic interaction terms as calculated in the Breit approximation. In this approximation, we: (i) evaluate the photon propagator in the Coulomb gauge, neglect (ii) the contribution of the negative energy continuum, as well as (iii) the energy dependence of the photon propagator, apart from its contribution to diagram (a) in Fig. 1. Whereas, the first-order contributions refer to diagrams (a) and (e) in this figure, the second-order terms include diagrams (b), (d), (f), and (g), respectively. As mentioned above, diagram (c) does not contribute if evaluated in the Coulomb gauge

within the Breit approximation. The next line $E_{Breit}^{\geq 3}$ then gives the contribution of the interelectronic interaction of the third and higher orders as outlined in Sec. II C. Besides the interelectronic interaction contributions, we also display the QED contributions in the various orders. As described above, the first order includes diagrams (a) and (f) from Fig. 2, whereas, the second order incorporates diagrams (b)–(e) and (g)–(j) in the same figure as well as the QED contributions of diagrams (b)–(d), (f), and (g) in Fig. 1. In line 7, we present estimates of the two-loop one-electron diagrams, and in line 8, we present the recoil correction. Finally, the total value of the transition energy is given in the last line.

As seen from this table, the overall transition energy converges very nicely to the value, which is almost independent of the particular screening potential used in the Dirac equation for representing the one-electron spectrum. For the case of boronlike fermium, the first-order QED contribution is smaller than the second-order QED term. This is due to a significant cancellation of the first-order VP and SE terms for this nuclear charge, similar as for the hydrogenlike ions for which the sum of the SE and VP terms for the $2p_{3/2}-2p_{1/2}$ transition is two orders of magnitude smaller than the individual terms themselves.

Table V displays the energies of the $2p_{3/2}-2p_{1/2}$ electric dipole forbidden transition for all boronlike ions with $17 \leq Z \leq 100$. These energies are the averages of the values as obtained for the four screening potentials. Within the rigorous treatment where the electron-electron interaction and QED corrections are taken for all orders, the transition energy should be fully independent of the particular screening potential. The discrepancy between the averaged value E_{theo} and the predictions, obtained for different potentials, can, therefore, provide an estimate of the neglected QED contributions. Alternatively, the uncertainty due to uncalculated QED contributions of the third- and higher-order terms can be conservatively estimated as the double ratio of the second-order QED contribution to the corresponding contribution obtained within the Breit approximation E_{QED}^2/E_{Breit}^2 , multiplied with $E_{Breit}^{\geq 3}$. The maximal value of both estimates is quadratically summed with the uncertainties of the other contributions, and the obtained value is taken as the theoretical uncertainty in Tables V and VI.

In Table VI, finally, we compare our theoretical $2p_{3/2}-2p_{1/2}$ transition energies with the previous calculations by Safronova and co-workers [31] and with available experimental data. Overall good agreement is found for almost all elements with the computations of Ref. [31] in which the QED contributions have been estimated semiempirically, whereas, in some cases, there exist deviations with regard to experiment. This might not be surprising since, apart from the experiments with boronlike argon [1–3], all other energies were obtained more than 20 years ago from astrophysical data or TOKAMAK plasma observations. We hope that the present computations will renew interest in the accurate measurements of the $2p_{3/2}-2p_{1/2}$ dipole-forbidden transitions based on new experimental techniques; see Ref. [4] for a recent review on this topic.

V. SUMMARY

To summarize, we have performed accurate calculations of the $2p_{3/2}-2p_{1/2}$ transition energies for all boronlike ions with

TABLE V. Theoretical energies (in eV) for the $2p_{3/2} - 2p_{1/2}$ forbidden transition in boronlike ions with $17 \leq Z \leq 100$.

Ion	E_{theo}	Ion	E_{theo}	Ion	E_{theo}	Ion	E_{theo}
Cl ¹²⁺	2.1593(4)	Sr ³³⁺	77.3249(72)	Pr ⁵⁴⁺	529.577(27)	Hg ⁷⁵⁺	2097.13(13)
Ar ¹³⁺	2.8091(4)	Y ³⁴⁺	86.5888(78)	Nd ⁵⁵⁺	570.473(28)	Tl ⁷⁶⁺	2222.42(14)
K ¹⁴⁺	3.5976(5)	Zr ³⁵⁺	96.6835(84)	Pm ⁵⁶⁺	613.845(29)	Pb ⁷⁷⁺	2354.01(16)
Ca ¹⁵⁺	4.5411(5)	Nb ³⁶⁺	107.6608(91)	Sm ⁵⁷⁺	659.810(30)	Bi ⁷⁸⁺	2492.20(17)
Sc ¹⁶⁺	5.6602(8)	Mo ³⁷⁺	119.5750(98)	Eu ⁵⁸⁺	708.494(31)	P ⁷⁹⁺	2637.29(19)
Ti ¹⁷⁺	6.9756(11)	Tc ³⁸⁺	132.483(10)	Gd ⁵⁹⁺	760.018(33)	At ⁸⁰⁺	2789.59(21)
V ¹⁸⁺	8.5100(15)	Ru ³⁹⁺	146.442(11)	Tb ⁶⁰⁺	814.520(36)	Rn ⁸¹⁺	2949.38(23)
Cr ¹⁹⁺	10.2867(19)	Rh ⁴⁰⁺	161.513(12)	Dy ⁶¹⁺	872.125(38)	Fr ⁸²⁺	3117.14(25)
Mn ²⁰⁺	12.3308(23)	Pd ⁴¹⁺	177.761(12)	Ho ⁶²⁺	932.985(41)	Ra ⁸³⁺	3293.13(28)
Fe ²¹⁺	14.6686(27)	Ag ⁴²⁺	195.249(13)	Er ⁶³⁺	997.246(45)	Ac ⁸⁴⁺	3477.77(31)
Co ²²⁺	17.3278(27)	Cd ⁴³⁺	214.047(14)	Tm ⁶⁴⁺	1065.062(48)	Th ⁸⁵⁺	3671.44(34)
Ni ²³⁺	20.3379(27)	In ⁴⁴⁺	234.223(14)	Yb ⁶⁵⁺	1136.590(52)	Pa ⁸⁶⁺	3874.64(37)
Cu ²⁴⁺	23.7300(28)	Sn ⁴⁵⁺	255.855(15)	Lu ⁶⁶⁺	1212.001(55)	U ⁸⁷⁺	4087.59(41)
Zn ²⁵⁺	27.5364(30)	Sb ⁴⁶⁺	279.016(16)	Hf ⁶⁷⁺	1291.485(59)	Np ⁸⁸⁺	4311.16(46)
Ga ²⁶⁺	31.7914(35)	Te ⁴⁷⁺	303.787(17)	Ta ⁶⁸⁺	1375.193(63)	Pu ⁸⁹⁺	4545.62(50)
Ge ²⁷⁺	36.5304(41)	I ⁴⁸⁺	330.248(18)	W ⁶⁹⁺	1463.342(69)	Am ⁹⁰⁺	4791.48(56)
As ²⁸⁺	41.7899(46)	Xe ⁴⁹⁺	358.487(19)	Re ⁷⁰⁺	1556.128(76)	Cm ⁹¹⁺	5049.54(63)
Se ²⁹⁺	47.6094(51)	Cs ⁵⁰⁺	388.593(21)	Os ⁷¹⁺	1653.742(84)	Bk ⁹²⁺	5320.16(70)
Br ³⁰⁺	54.0292(56)	Ba ⁵¹⁺	420.656(22)	Ir ⁷²⁺	1756.424(94)	Cf ⁹³⁺	5604.00(79)
Kr ³¹⁺	61.0920(62)	La ⁵²⁺	454.774(24)	Pt ⁷³⁺	1864.39(10)	Es ⁹⁴⁺	5901.77(89)
Rb ³²⁺	68.8419(67)	Ce ⁵³⁺	491.047(25)	Au ⁷⁴⁺	1977.87(12)	Fm ⁹⁵⁺	6214.2(1.0)

$17 \leq Z \leq 100$. A computational scheme has been worked out to rigorously evaluate the QED contributions for many-electron ions. Good agreement with previous computations and accurate measurements is found. This paper clearly improves the available database for boronlike ions.

ACKNOWLEDGMENTS

We would like to thank Dr. J. R. Crespo López-Urrutia and Dr. V. A. Yerokhin for valuable discussions during the work on the paper. The work of V.M.S. and I.I.T. was supported by RFBR (Grant No. 13-02-00630) and by the Ministry of Education and Science of the Russian Federation (Grant No. 8420). A.N.A. and A.S. acknowledge support by the

Helmholtz Association under Project No. VH-NG-421. The work of A.N.A. was also supported by the German Research Foundation (DFG) within the Emmy Noether program under Contract No. TA 740 1-1.

APPENDIX: EVALUATION OF THE FIRST- AND SECOND-ORDER CORRECTIONS TO THE FREE-ELECTRON GREEN'S FUNCTION

In this Appendix, we present the numerical procedure for calculating the first- and second-order corrections for the free-electron Green's function owing to the interaction of the electron with an external potential. The free-electron Green's function can be written in the following form:

$$G(\omega; \mathbf{x}, \mathbf{y}) = \sum_{\kappa, m} \begin{bmatrix} G_{\kappa}^{11}(\omega; x, y) \Omega_{\kappa m}(\hat{\mathbf{x}}) \Omega_{\kappa m}^{\dagger}(\hat{\mathbf{y}}) & -i G_{\kappa}^{12}(\omega; x, y) \Omega_{\kappa m}(\hat{\mathbf{x}}) \Omega_{-\kappa m}^{\dagger}(\hat{\mathbf{y}}) \\ i G_{\kappa}^{21}(\omega; x, y) \Omega_{-\kappa m}(\hat{\mathbf{x}}) \Omega_{\kappa m}^{\dagger}(\hat{\mathbf{y}}) & G_{\kappa}^{22}(\omega; x, y) \Omega_{-\kappa m}(\hat{\mathbf{x}}) \Omega_{-\kappa m}^{\dagger}(\hat{\mathbf{y}}) \end{bmatrix}, \quad (A1)$$

where $\Omega_{\kappa m}$ are spherical spinors and G^{ik} are the radial Green's function components. These components can be expressed in terms of the spherical Bessel functions and the spherical Hankel functions of the first kind. For $x > y$, these radial components can be written as [8]

$$G_{\kappa}^{11} = (\omega + 1) c j_{|\kappa+1/2|-1/2}(icy) h_{|\kappa+1/2|-1/2}^{(1)}(icx),$$

$$G_{\kappa}^{12} = c^2 \frac{\kappa}{|\kappa|} j_{|\kappa+1/2|-1/2}(icy) h_{|\kappa-1/2|-1/2}^{(1)}(icx),$$

$$G_{\kappa}^{21} = c^2 \frac{\kappa}{|\kappa|} j_{|\kappa-1/2|-1/2}(icy) h_{|\kappa+1/2|-1/2}^{(1)}(icx), \quad (A2)$$

$$G_{\kappa}^{22} = (\omega - 1) c j_{|\kappa-1/2|-1/2}(icy) h_{|\kappa-1/2|-1/2}^{(1)}(icx),$$

$$c = \sqrt{1 - \omega^2}.$$

For the case of $x < y$, the radial components can be obtained from the relation $G^{ik}(\omega; \mathbf{x}, \mathbf{y}) = G^{ki}(\omega; \mathbf{y}, \mathbf{x})$. We suppose $x > y$ throughout this Appendix. Our goal here is to evaluate the first- and the second-order corrections to this Green's function owing to the interaction of the electron with an external

TABLE VI. Comparison of our theoretical $2p_{3/2}$ - $2p_{1/2}$ transition energies with previous calculations from Ref. [31] and experiment for selected elements along the boron isoelectronic sequence. All energies are given in eV, and estimated uncertainties are shown in parentheses.

Ion	E_{theo}	Ref. [31]	Experiment	Reference
Cl ¹²⁺	2.1593(4)	2.1604	2.1583(25)	[32]
Ar ¹³⁺	2.8091(4)	2.8107	2.8090279(6)	[1]
K ¹⁴⁺	3.5976(5)	3.5983	3.5963(31)	[32]
Ca ¹⁵⁺	4.5411(5)	4.5417	4.5397(37)	[32]
Sc ¹⁶⁺	5.6602(8)	5.6603	5.6583(4)	[33]
Ti ¹⁷⁺	6.9756(11)	6.9754	6.9732(4)	[34]
V ¹⁸⁺	8.5100(15)	8.5089	8.5061(50)	[32]
Cr ¹⁹⁺	10.2867(19)	10.285	10.2815(17)	[34]
Mn ²⁰⁺	12.3308(23)	12.327	12.3100(12)	[32]
Fe ²¹⁺	14.6686(27)	14.663	14.6640(35)	[34]
Co ²²⁺	17.3278(27)	17.321		
Ni ²³⁺	20.3379(27)	20.330	20.3286(68)	[34]
Cu ²⁴⁺	23.7300(28)	23.720	23.7154(93)	[34]
Zn ²⁵⁺	27.5364(30)	27.525		
Ge ²⁷⁺	36.5304(41)	36.513		
Kr ³¹⁺	61.0920(62)	61.061		
Zr ³⁵⁺	96.6835(84)	96.632		
Mo ³⁷⁺	119.5750(98)	119.511		
Ag ⁴²⁺	195.249(13)	195.145		
Sn ⁴⁵⁺	255.855(15)	255.722		
Xe ⁴⁹⁺	358.487(19)	358.303		
Nd ⁵⁵⁺	570.473(28)	570.197		
Eu ⁵⁸⁺	708.494(31)	708.168		
Yb ⁶⁵⁺	1136.590(52)	1136.117		
W ⁶⁹⁺	1463.342(69)	1462.762		
Au ⁷⁴⁺	1977.87(12)	1977.134		
Hg ⁷⁵⁺	2097.13(13)	2096.356		
Bi ⁷⁸⁺	2492.20(17)	2491.339		
Th ⁸⁵⁺	3671.44(34)	3670.227		
U ⁸⁷⁺	4087.59(41)	4086.394		
Fm ⁹⁵⁺	6214.2(1.0)	6212.580		

potential. Let us start with the first-order correction,

$$G^{(1)}(\omega; \mathbf{x}, \mathbf{y}) = \int d\mathbf{z} G(\omega; \mathbf{x}, \mathbf{z}) V(\mathbf{z}) G(\omega; \mathbf{z}, \mathbf{y}) \quad (\text{A3})$$

for which the angular integration can readily be performed due to the orthonormality of the spherical spinors. For the radial integration, in contrast, it is convenient to introduce a new shorthand notation,

$$A_{ik} = \begin{cases} (\omega + 1)c, & i = 1, \quad k = 1, \\ c^2 \frac{\kappa}{|\kappa|}, & i = 1, \quad k = 2, \\ c^2 \frac{\kappa}{|\kappa|}, & i = 2, \quad k = 1, \\ (\omega - 1)c, & i = 2, \quad k = 2. \end{cases} \quad (\text{A4})$$

Moreover, instead of specifying the order of the spherical Bessel and Hankel functions explicitly, we will simply use the notation j_{ik} and h_{ik} where the particular order of these functions can be obtained from Eq. (A2). With these notations,

we get

$$G_{\kappa}^{(1)ik} = \sum_{m=1}^2 A_{im} A_{mk} \left(h_{im}(icx), h_{km}(icy) \right. \\ \times \int_0^y z^2 dz j_{im}(icz) j_{km}(icz) V(z) \\ + h_{im}(icx) j_{mk}(icy) \int_y^x z^2 dz j_{im}(icz) h_{mk}(icz) V(z) \\ + j_{mi}(icx) j_{mk}(icy) \\ \left. \times \int_x^{\infty} z^2 dz h_{mi}(icz) h_{mk}(icz) V(z) \right). \quad (\text{A5})$$

As seen from this expression, the summands in Eq. (A5) have the same form. Namely, a prefactor which does not depend on the coordinates x and y is multiplied with the sum of three terms. Each of these terms is a product of two Bessel or Hankel functions and an integral over the product of two Bessel or Hankel functions and the external potential. We note here that each term just contains two Bessel and two Hankel functions that guarantee the correct behavior at long and short distances.

In practice, we are interested in the values of $G_{\kappa}^{(1)}$ at given points $\{x_i\}$ and $\{y_i\}$ as defined by the integration mesh over x and y . If one can precalculate and can store these functions at the mesh, the components of $G^{(1)}$ are calculated rather quickly. Moreover, because every term in Eq. (A5) is a product of two functions, one depending on x and the other on y , there is no need to store the functions on a two-dimensional grid. A one-dimensional grid is just enough in this case.

As an example, let us consider one term in Eq. (A5),

$$T = h_{im}(icx) j_{mk}(icy) \int_y^x z^2 dz j_{im}(icz) h_{mk}(icz) V(z). \quad (\text{A6})$$

First of all, let us rewrite it in the form

$$T = h_{im}(icx) j_{mk}(icy) \left(\int_0^x z^2 dz j_{im}(icz) h_{mk}(icz) V(z) \right. \\ \left. - \int_0^y z^2 dz j_{im}(icz) h_{mk}(icz) V(z) \right). \quad (\text{A7})$$

Now, it is clear that, for a quick calculation of this term at a given energy, the following functions should be stored on a one-dimensional grid: (i) the functions $j_{mk}(icx)$, (ii) the functions $h_{mk}(icx)$, and (iii) the values of the integral $\int_0^x z^2 dz j_{im}(icz) h_{mk}(icz) V(z)$ as a function of the upper integration limit x . In addition, for the evaluation of the other terms in Eq. (A5), one needs the values of the integrals $\int_0^x z^2 dz j_{im}(icz) j_{mk}(icz) V(z)$ and $\int_x^{\infty} z^2 dz h_{im}(icz) h_{mk}(icz) V(z)$ as functions of the upper (lower) integration limit. Once these functions are stored on the grid, the calculation of $G_{\kappa}^{(1)}$ is very fast at any given point (x, y) .

Owing to the fast oscillation of the Green's function components for large *real* values of ω , the integration contour for evaluating the self-energy correction by means of formula (6) usually is rotated in order to be parallel to the imaginary axis. In our calculations, we, therefore, transform the expression (6)

into the form

$$\langle a|\Sigma(\epsilon)|b\rangle = \frac{i}{2\pi} \int_{-\infty}^{\infty} d\omega \times \sum_n \frac{\langle an|e^{2\alpha^\mu}\alpha^\nu D_{\mu\nu}(\epsilon - \omega)|nb\rangle}{\omega - \epsilon_n(1 - i0)}, \quad (\text{A8})$$

and then rotate the contour directly upon the imaginary axis. This rotation has the advantage that the complex phase of the Bessel and Hankel functions j_{ik} and h_{ik} remains constant and is equal to $N\pi/2$ with N being an integer. This particular property allows a much faster calculation. Moreover, for an imaginary energy, the absolute values of the Bessel and Hankel functions either grow or vanish exponentially as the radial variable is increased and behave like r^l and r^{-l-1} for $r \rightarrow 0$, correspondingly. This behavior of the Bessel and Hankel functions makes it impossible to directly store their values and/or integrals at the radial mesh, whereas, the logarithms of these functions can still be kept in memory at sufficiently small and large values of r . Instead of the direct evaluation of three terms in Eq. (A5), we, therefore, evaluate and store their logarithms. For the Bessel and Hankel functions, the logarithms can be computed directly, whereas, the formulas for the numerical integration need to be rewritten in order to evaluate the logarithms of the integrals in Eq. (A5).

Typically, the formula,

$$I = \sum_{i=1}^N w_i f(x_i) \quad (\text{A9})$$

is used for numerical integration over a given grid. Here, I is the (numerical) value of the integral, f is the integrand, N is the number of knots, and w_i and x_i represent the integration weights and knots, respectively. The particular values of the weights and knots depend on the quadrature formula used for the integration. In the present paper, we have applied the Gauss-Legendre quadrature with eight knots. If we are now interested in the value of $\ln I$ (instead of I), we can use the

well-known addition theorem for logarithms,

$$\ln(B + C) = \ln B + \ln[1 + \exp(\ln C - \ln B)], \quad (\text{A10})$$

in order to evaluate the logarithm of the sum of two almost arbitrary large (or small) values with high accuracy. Using Eq. (A10), we can rewrite formula (A9) as

$$I = S_N, \quad (\text{A11})$$

with

$$S_k = \sum_{i=1}^k w_i f(x_i), \quad (\text{A12})$$

and to calculate the value S_N recursively. To this end, we first compute the value of $\ln S_1$ and then use Eq. (A10) in the form

$$\begin{aligned} \ln(S_{k+1}) &= \ln(S_k) + \ln(1 + \exp\{\ln(w_{k+1}) \\ &\quad + \ln[f(x_{k+1})] - \ln(S_k)\}) \end{aligned} \quad (\text{A13})$$

to obtain S_N . Since the logarithms of the spherical Bessel and Hankel functions behave quite smoothly for all arguments, from very short to long distances, we can interpolate the values $\ln[f(x_k)]$ in Eq. (A13) from the already stored logarithms. For the computation of (the radial components of) $G^{(1)}$, finally, Eq. (A5) is applied for each value of ω by using the logarithms calculated before.

Once the first-order correction $G^{(1)}$ is obtained, the second-order correction to the free-electron Green's function can be calculated as an (two-dimensional) integral with regard to the two radial variables,

$$\begin{aligned} G^{(2)}(\omega; \mathbf{x}, \mathbf{y}) &= \int d\mathbf{z}_1 \int d\mathbf{z}_2 G(\omega; \mathbf{x}, \mathbf{z}_1) V(\mathbf{z}_1) \\ &\quad \times G(\omega; \mathbf{z}_1, \mathbf{z}_2) V(\mathbf{z}_2) G(\omega; \mathbf{z}_2, \mathbf{y}). \end{aligned} \quad (\text{A14})$$

The procedure for calculating this second-order correction is essentially the same as before. In addition to the logarithms of the Bessel and Hankel functions and the one-dimensional integrals at the given radial mesh, we now need to store the logarithms of some two-dimensional radial integrals. The evaluation of the $G^{(2)}$ contributions is then performed by using the formula,

$$\begin{aligned} G^{(2)ik} &= \sum_{m,n=1}^2 A_{im} A_{mn} A_{nk} \left(h_{im}(icx) h_{kn}(icy) \int_0^y dz_1 z_1^2 V(z_1) j_{im}(icz_1) h_{mn}(icz_1) \int_0^{z_1} dz_2 z_2^2 V(z_2) j_{kn}(icz_2) j_{mn}(icz_2) \right. \\ &\quad + h_{im}(icx) h_{kn}(icy) \int_0^y dz_1 z_1^2 V(z_1) j_{im}(icz_1) j_{nm}(icz_1) \int_{z_1}^y dz_2 z_2^2 V(z_2) h_{nm}(icz_2) j_{kn}(icz_2) \\ &\quad + h_{im}(icx) j_{nk}(icy) \int_0^y dz_1 z_1^2 V(z_1) j_{im}(icz_1) j_{nm}(icz_1) \int_y^\infty dz_2 z_2^2 V(z_2) h_{nm}(icz_2) h_{nk}(icz_2) \\ &\quad + h_{im}(icx) h_{kn}(icy) \int_y^x dz_1 z_1^2 V(z_1) j_{im}(icz_1) h_{mn}(icz_1) \int_0^y dz_2 z_2^2 V(z_2) j_{kn}(icz_2) j_{mn}(icz_2) \\ &\quad + h_{im}(icx) j_{nk}(icy) \int_y^x dz_1 z_1^2 V(z_1) j_{im}(icz_1) h_{mn}(icz_1) \int_y^{z_1} dz_2 z_2^2 V(z_2) j_{mn}(icz_2) h_{nk}(icz_2) \\ &\quad + h_{im}(icx) j_{nk}(icy) \int_y^x dz_1 z_1^2 V(z_1) j_{im}(icz_1) j_{nm}(icz_1) \int_{z_1}^\infty dz_2 z_2^2 V(z_2) h_{nm}(icz_2) h_{nk}(icz_2) \\ &\quad \left. + j_{mi}(icx) h_{kn}(icy) \int_x^\infty dz_1 z_1^2 V(z_1) h_{mi}(icz_1) h_{mn}(icz_1) \int_0^y dz_2 z_2^2 V(z_2) j_{mn}(icz_2) j_{kn}(icz_2) \right) \end{aligned}$$

$$\begin{aligned}
& + j_{mi}(icx)j_{nk}(icy) \int_x^\infty dz_1 z_1^2 V(z_1) h_{mi}(icz_1) h_{mn}(icz_1) \int_y^{z_1} dz_2 z_2^2 V(z_2) j_{mn}(icz_2) h_{nk}(icz_2) \\
& + j_{mi}(icx)j_{nk}(icy) \int_x^\infty dz_1 z_1^2 V(z_1) h_{mi}(icz_1) j_{nm}(icz_1) \int_{z_1}^\infty dz_2 z_2^2 V(z_2) h_{nm}(icz_2) h_{nk}(icz_2) \Big). \quad (\text{A15})
\end{aligned}$$

At first glance, this formula looks quite complicated. However, if we take into account that the logarithms of the Bessel and Hankel functions as well as of all required one-dimensional integrals are already stored, one can interpolate these values and, therefore, the storage of the two-dimensional radial integrals is fast and just takes a few seconds for each energy.

The computational procedure outlined above has been tested for the $G^{(2)}$ contributions by comparing the obtained values with *direct* computation by formula (A14). The same procedure can be used with minor modifications in order to evaluate the other second-order diagrams in α for which the analytical solution for the Green's function is known.

-
- [1] I. Draganić, J. R. Crespo López-Urrutia, R. DuBois, S. Fritzsche, V. M. Shabaev, R. S. Orts, I. I. Tupitsyn, Y. Zou, and J. Ullrich, *Phys. Rev. Lett.* **91**, 183001 (2003).
- [2] R. Soria Orts, Z. Harman, J. R. Crespo López-Urrutia, A. N. Artemyev, H. Bruhns, A. J. González Martínez, U. D. Jentschura, C. H. Keitel, A. Lapierre, V. Mironov, V. M. Shabaev, H. Tawara, I. I. Tupitsyn, J. Ullrich, and A. V. Volotka, *Phys. Rev. Lett.* **97**, 103002 (2006).
- [3] V. Mäckel, R. Klawitter, G. Brenner, J. R. Crespo López-Urrutia, and J. Ullrich, *Phys. Rev. Lett.* **107**, 143002 (2011).
- [4] M. Vogel and W. Quint, *J. Phys. B* **42**, 154016 (2009).
- [5] A. N. Artemyev, V. M. Shabaev, I. I. Tupitsyn, G. Plunien, and V. A. Yerokhin, *Phys. Rev. Lett.* **98**, 173004 (2007).
- [6] V. A. Yerokhin, A. N. Artemyev, V. M. Shabaev, M. M. Sysak, O. M. Zherebtsov, and G. Soff, *Phys. Rev. A* **64**, 032109 (2001).
- [7] P. J. Mohr, *Ann. Phys. (NY)* **88**, 26 (1974).
- [8] P. J. Mohr, *Ann. Phys. (NY)* **88**, 52 (1974).
- [9] G. Soff and P. J. Mohr, *Phys. Rev. A* **38**, 5066 (1988).
- [10] N. L. Manakov, A. A. Nekipelov and A. G. Fainshtein, *Zh. Eksp. Teor. Fiz.* **95**, 1167 (1989) [*Sov. Phys. JETP* **68**, 673 (1989)].
- [11] N. J. Snyderman, *Ann. Phys. (NY)* **211**, 43 (1991).
- [12] S. A. Blundell and N. J. Snyderman, *Phys. Rev. A* **44**, R1427 (1991).
- [13] E. A. Uehling, *Phys. Rev.* **48**, 55 (1935).
- [14] A. N. Artemyev, V. M. Shabaev, V. A. Yerokhin, G. Plunien, and G. Soff, *Phys. Rev. A* **71**, 062104 (2005).
- [15] V. M. Shabaev, *Phys. Rep.* **356**, 119 (2002).
- [16] V. F. Bratsev, G. B. Deyneka, and I. I. Tupitsyn, *Bull. Acad. Sci. USSR, Phys. Ser.* **41**, 173 (1977).
- [17] V. A. Yerokhin, P. Indelicato, and V. M. Shabaev, *Phys. Rev. Lett.* **97**, 253004 (2006).
- [18] V. A. Yerokhin, P. Indelicato, and V. M. Shabaev, *Phys. Rev. A* **77**, 062510 (2008).
- [19] U. D. Jentschura, A. Czarnecki, and K. Pachucki, *Phys. Rev. A* **72**, 062102 (2005).
- [20] V. M. Shabaev, I. I. Tupitsyn, K. Pachucki, G. Plunien, and V. A. Yerokhin, *Phys. Rev. A* **72**, 062105 (2005).
- [21] J. P. Perdew and A. Zunger, *Phys. Rev. B* **23**, 5048 (1981).
- [22] J. C. Slater, *Phys. Rev.* **81**, 385 (1951).
- [23] R. Latter, *Phys. Rev.* **99**, 510 (1955).
- [24] W. R. Johnson, S. A. Blundell, and J. Sapirstein, *Phys. Rev. A* **37**, 307 (1988).
- [25] V. M. Shabaev, I. I. Tupitsyn, V. A. Yerokhin, G. Plunien, and G. Soff, *Phys. Rev. Lett.* **93**, 130405 (2004).
- [26] V. A. Yerokhin and V. M. Shabaev, *Phys. Rev. A* **60**, 800 (1999).
- [27] P. J. Mohr, *Phys. Rev. A* **46**, 4421 (1992).
- [28] A. N. Artemyev, V. M. Shabaev, and V. A. Yerokhin, *Phys. Rev. A* **56**, 3529 (1997).
- [29] A. N. Artemyev, T. Beier, G. Plunien, V. M. Shabaev, G. Soff, and V. A. Yerokhin, *Phys. Rev. A* **60**, 45 (1999).
- [30] V. A. Yerokhin, A. N. Artemyev, T. Beier, G. Plunien, V. M. Shabaev, and G. Soff, *Phys. Rev. A* **60**, 3522 (1999).
- [31] M. S. Safronova, W. R. Johnson, and U. I. Safronova, *Phys. Rev. A* **54**, 2850 (1996).
- [32] B. Edlén, *Phys. Scr.* **28**, 483 (1983).
- [33] S. Suckewer, J. Cecchi, S. Cohen, R. Fonck, and E. Hinnov, *Phys. Lett. A* **80**, 259 (1980).
- [34] E. Hinnov, S. Suckewer, S. Cohen, and K. Sato, *Phys. Rev. A* **25**, 2293 (1982).